Available online at www.keaipublishing.com/en/journals/journal-of-magnesium-and-alloys/

ScienceDirect

Journal of Magnesium and Alloys 15 (2026) 101947

www.elsevier.com/locate/jma

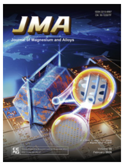

Full Length Article

Local mechanical behavior and enhanced ductility of ultrastrongly textured AM50 rods processed via constrained friction processing

Camila Caroline de Castro[a,*], Ting Chen[b], Diogo de Campos Fernandes[b,c],
Benjamin Klusemann[a,b]

[a] *Leuphana University Lüneburg, Institute for Production Technology and Systems, 21335 Lüneburg, Germany*
[b] *Helmholtz-Zentrum Hereon, Institute of Material and Process Design, Solid-State Materials Processing, 21502 Geesthacht, Germany*
[c] *Federal University of São Carlos, Department of Materials Engineering, 13565-905 São Carlos, Brazil*

Received 14 August 2025; received in revised form 18 October 2025; accepted 5 November 2025
Available online 6 January 2026

Abstract

Constrained friction processing (CFP) is an innovative technique for lightweight materials, producing fine or ultrafine microstructures through severe plastic deformation. CFP favors the formation of ultrastrong B-fiber texture in rods of Mg alloys, with its orientations varying along the rod according to the local material flow conditions. This study aims to investigate the local micromechanical behavior of AM50 rods produced via CFP and the deformation mechanisms under tensile loading specific to each analyzed position. For this purpose, a combined analysis of local microstructure and microindentation was performed, followed by tensile testing of micro-flat specimens taken at three rod positions, i.e. center and edge along the plunge direction, and middle along the radial direction, in order to investigate the role of grain size and texture on the local deformation mechanisms, and ultimately, the local mechanical properties. The results indicate that texture has a more dominant influence than grain size on the local mechanical behavior of rods processed via CFP given the pronounced gradient of ultrastrong textures observed along the rod radius, which determines the dominant deformation mechanisms. Furthermore, an approach using quasi-in-situ tensile tests performed at the center of the rod indicates that slip and tensile twinning are the main deformation modes for the ultrastrong B-fiber texture observed at this position. In contrast, at the middle of the rod, the deformation of the local ultrastrong basal texture is ruled by basal $\langle a \rangle$ slip, combined to the slip transfer. An exceptional enhancement in elongation at break (≈49 %) is observed in the sample taken at the edge of the rod, with an ultrastrong B-fiber texture tilted 25° in relation to the center. This is attributed to a combination of lattice rotation, which aligns the basal planes at 45° to the tensile axis, and the maximized activity of basal $\langle a \rangle$ slip.

Keywords: Magnesium alloy; Constrained friction processing; Local mechanical behavior; Quasi-in-situ tensile tests; Enhanced ductility.

1. Introduction

Constrained Friction Processing (CFP) is an innovative friction-based extrusion technique [10], applicable for processing lightweight materials like Al and Mg alloys. This process employs a thermo-mechanical approach that involves the severe plastic deformation (SPD) of the material being processed. CFP is a new alternative to produce extrudates based on the version of the well-established refill friction stir spot welding (refill FSSW) process [43]. Like other thermo-mechanical processing methods involving SPD, CFP is an interesting option for producing extrudates with refined microstructures from Mg alloys. As demonstrated by Chen et al. [12], the CFP of the ZX00 Mg-Zn-Ca alloy can produce microstructures with grain sizes of around 5–6 μm, resulting in improved compressive yield strength and ultimate compressive strength [13] in comparison to other extrusion methods [6]. In addition to this microstructure refinement, CFP shows several advantages over other thermo-mechanical techniques. Contrary to other SPD processes like equal channel angular pressing (ECAP) [11,42,53], simple shear extru-

---

Peer review under the responsibility of Chongqing University.
* Corresponding author.
E-mail address: camila.castro@leuphana.de (C.C. de Castro).

https://doi.org/10.1016/j.jma.2025.11.007

sion (SSE) [42], accumulative roll bonding (ARB) [25] and multi-directional forging (MDF) [54], which require the preheating of the material, CFP eliminates the necessity of this pre-processing step as the heat generation is intrinsic to the process, resulting from the combination of friction and plastic deformation [9]. Furthermore, the presence of the probe and its effects on the processability – and consequently the resulting microstructure – is an advantage in comparison to other friction-based extrusion processes like friction extrusion [2,41]. In contrast, the current limitations in size capabilities associated with the existing refill FSSW equipment may restrict the applicability of CFP to small rods.

The specific local shearing conditions imposed by the CFP on the material being processed clearly affect the crystallographic orientation of the grains. This is especially true for Mg alloys, given the anisotropic nature of their hexagonal close-packed (hcp) structure. For instance, conventional extrusion is reported to induce a texture in which the basal planes align with the extrusion direction [39], whereas ECAP produces textures where the c-axis is oriented perpendicular to the extrusion plane [18]. In the case of CFP, the local texture is extremely influenced by the material flow, resulting in a B-fiber texture aligned with the plunge direction at the center of the rod, which progressively tilts in direction to the radial direction for positions closer to the border [10]. Although the texture intensity produced by extrusion [39], ECAP [18] and high-pressure torsion (HPT) [51] are referred as‘strong basal textures’ up to 14 multiple times random (mrd), the crystallographic orientation intensity in CFP can be classified as an ‘ultrastrong texture’, with values reported as high as 90 mrd [13]. This texture intensity range is consistent with the resultant crystallographic orientation of Mg alloys processed by other friction-based methods, like refill FSSW (up to 75 mrd) [17] and friction stir welding (FSW) (43 mrd) [45].

The main deformation mode in single crystals of Mg and its alloys is dislocation slip, which occurs in particular slip systems. The activation of basal $\langle a\rangle$ slip is the most energetically favorable as it corresponds to the lowest critical resolved shear stress (τ_{crss}) of Mg slip systems [5]. At room temperature, this is the only dislocation system that can be activated. The Schmid's law, schematically represented in Fig. 1 and defined as

$$\tau_R = \sigma_{app} \cdot SF = \sigma_{app} \cdot \cos\phi \, \cos\lambda \tag{1}$$

correlates the resolved shear stress (τ_R) and the applied stress (σ_{app}) based on the angle between the vector normal to the slip plane (ϕ) and the angle with the slip direction (λ), referred to as the Schmid factor (SF). The SF is a good estimation of the preferential slip systems to be activated under a given load. In the case of materials with strong basal texture under tensile loading, like extruded bars or rolled plates in which σ_{app} // (0001), the majority of the grains are oriented such that $\phi \approx 90^\circ$ and $0^\circ \leq \lambda \leq 30^\circ$. This results in low SF and high τ_R values needed to activate basal $\langle a\rangle$ dislocations, which directly contribute to the low ductility observed in these materials.

Twinning is observed as an additional deformation mechanism activated when slip is restricted. In materials such as Mg-[14], Zn- [21], and Ti [48] alloys, this additional mechanism can be activated due to the limited number of slip systems intrinsic to the hcp structure as previously discussed. Nonetheless, besides accommodating strain through the displacement of the mirror lattice symmetry, twinning also promotes the nucleation and growth of the fraction of the material with crystallographic orientations that may favor slip systems activated under lower τ_{crss} relative to the tensile/compression axis [7]. Independent twinning systems are activated in response to the direction of the applied load. Under tensile loading along the c-axis of the hcp structure, the dominant twinning system is the $\{10\bar{1}2\}$, followed by $\{11\bar{2}1\}$, while under compression, the main twinning system is $\{10\bar{1}1\}$, in addition to $\{11\bar{2}2\}$. In each case, the twin boundary inherits a specific misorientation: $\sim 86^\circ$ for $\{10\bar{1}2\}$ [3], $\sim 35^\circ$ for $\{11\bar{2}1\}$ [48], $\sim 56^\circ$ for $\{10\bar{1}1\}$ [4], and $\sim 64^\circ$ for $\{11\bar{2}2\}$ [48].

This study investigates the influence of local microstructural features determined by the material flow during the CFP of AM50 rods on the local mechanical behavior, with a focus on the effect of the characteristic ultrastrong crystallographic orientation. For this purpose, the influence of grain size and texture on local indentation patterns along the rod is analyzed, followed by microtensile experiments using a quasi-in-situ approach at successive deformation levels, in order to un-

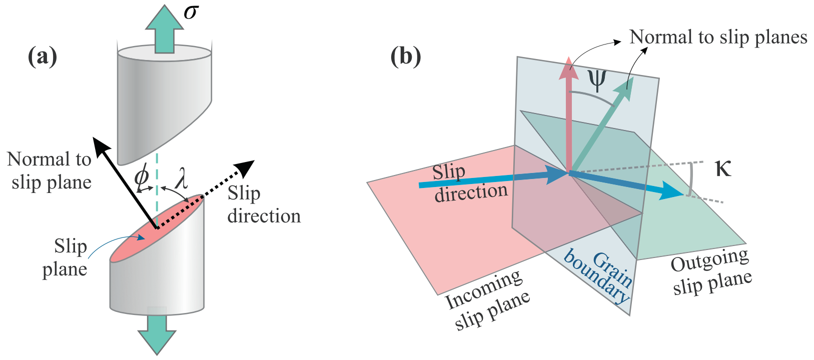

Fig. 1. Geometric relationships between the tensile axis, slip plane and slip direction defining the (a) Schmid factor (SF) and (b) geometric compatibility factor (m').

derstand the changes in the resulting grain structure at three positions along the rod and the corresponding deformation mechanisms. This investigation establishes a basis for tailoring the material flow components during the CFP to produce the desired textures. In this way, control over dominant deformation mechanisms can be enabled, optimizing key properties such as strength and ductility in Mg alloys to meet the requirements of targeted applications.

2. Materials and methods

2.1. Process principle

A representation of the CFP process steps is depicted in Fig. 2. In (a), the toolset approaches the plate to be processed, and the clamping ring applies the set clamping force to the system as the shoulder and probe begin to rotate. Next, in (b) the rotating shoulder plunges into the base material (BM), causing its extrusion to the hollow cavity inside the shoulder created by the progressive retraction of the probe, which generates a spiral-like material flow. By the action of the probe, this material flow is constrained, which enhances the transmission of the shearing to the material being processed and prevents the occurrence of voids. As the set plunge depth is reached (c), the rotation of the tool parts halts, when the retraction of the shoulder is activated, terminating the contact with the processed rod. The process is finished with the release of the clamping force, leaving the rod as illustrated in (d).

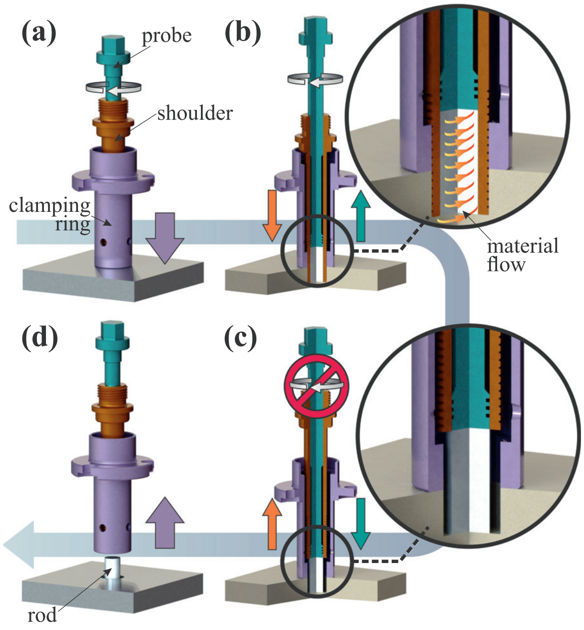

Fig. 2. Step-by-step schematic representation of constrained friction processing (CFP): (a) loading, (b) plunging, (c) rotation halt followed by shoulder retraction and (d) release of the processed rod. The three-part toolset consists of the clamping ring (purple), shoulder (orange) and probe (green).

2.2. Processing of rods and production of specimens

Ingots of AM50 alloy (94.24 wt% Mg, 5.21 wt% Al, 0.47 wt% Mn, 0.05 wt% Zn, 0.03 wt% Si, 0.002 wt% Cu, 0.001 wt% Fe) cast via Permanent Mold Casting [16] were cut into workpieces with 100 x 25 x 6 mm^3 to be used as the base material for further processing. Rods with the dimensions presented in Table 1 were produced via CFP using the custom-designed RPS200 refill FSSW system (Harms & Wende, Germany) operated by position control using clamping rings and probes made of M4 tool-steel and G40 tungsten carbide shoulders. The combination of parameters, i.e. rotational speed (RS), plunge speed (PS), dwell time (DT) and clamping force (CF), as well as the dimension of tool parts used for each experiment are listed in Table 1. While process parameters for microtensile investigation were obtained from previous investigations [10], Vickers indentations were performed on a rod with a larger diameter in order to increase the number of data points collected along the radius, following preliminary parameter optimization using a ∅12 shoulder.

2.3. Microstructure and texture analysis

Electron backscatter diffraction (EBSD) analyses were performed using a FEI Quanta 650 FEG scanning electron microscope (SEM) equipped with an EDAX Velocity EBSD detector, operated using 20 kV using a step size of 0.2 µm. For this purpose, one micro-flat specimen of each configuration was embedded in acrylic resin and polished down to 0.2 µm using a water-free fumed silica suspension. Once the desired surface quality was achieved, the micro-flat samples were carefully released from the resin by soaking in acetone, which allowed for their safe removal without compromising the polished surface. The acquired EBSD data were primarily analyzed using the TSL OIM 7.3 software, applying a minimum boundary misorientation cut-off of 2° to eliminate orientation noise artifacts, and a 15° misorientation threshold between adjacent grains to define high-angle grain boundaries. Complementary crystallographic analyses, such as the construction of Schmid factor maps, slip traces and geometric compatibility factor maps, were performed using MATLAB combined with the MTEX toolbox [1].

2.4. Local mechanical properties

2.4.1. Local microtensile behavior and quasi-in-situ experiments

The local micromechanical behavior at three positions of the rod was determined using custom-designed micro-flat tensile specimens, produced according to the dimensions depicted in Fig. 3(a). The samples were cut via electrical discharge machining (EDM) wire erosion to prevent deformation and were taken at three positions of identically produced rods: at the middle along the radial direction (RD-middle), at the center along the plunge direction (PD-center), and at the edge along the plunge direction (PD-edge), as illustrated in Fig. 3(b).

Table 1
Dimension of produced rods, process parameters and dimensions of tool parts used in each experiment.

Rod		Process parameters				Tool dimensions [mm]		
∅ [mm]	h [mm]	RS [rpm]	PS [mm/s]	DT [s]	CF [kN]	Clamping ring	Shoulder	Probe
6	6.75	1800	1	0	12	∅17	∅9	∅6
8	6.75	1500	1.2	1.5	12	∅20	∅12	∅8

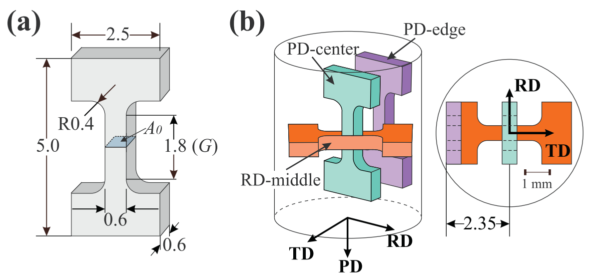

Fig. 3. Micro-flat specimens for tensile testing: (a) dimensions of the specimens and (b) positions of the produced samples in relation to the rod. In red, the specimen at the middle along the radial direction of the rod (RD-middle); in green, the specimen at the center along the plunge direction of the rod (PD-center); in purple, the sample at the edge along the plunge direction (PD-edge). PD, RD and TD are the coordinates defining the axis system, corresponding respectively to plunge direction, radial direction and transverse direction. All dimensions in mm.

Tensile tests were carried out at room temperature using a Deben Microtest 5 kN (Deben UK Ltd., United Kingdom) microtensile stage with a constant extension rate of 0.1 mm/min and applying a preload of 5 N. Three samples of each configuration were tested. The acquired data for force (F) and displacement (Δl) were used to calculate the engineering stress (σ_{app}) and strain (ε) according to ASTM E8M [26], in which $\sigma_{app}=F/A_0$ and $\varepsilon = \Delta l/G$, being A_0 and G respectively the initial cross-sectional area and gauge length, as defined in Fig. 3.

Quasi-in-situ experiments were used to monitor the effect of deformation in the grain structure of a single sample for each configuration using EBSD. With the exception of RD-middle, in which the highly deformed surface at ε_p=0.15 led to extremely low confidence index (CI) through all the sample, making meaningful interpretation of the results impossible, progressive strains were applied to each specimen in four distinct steps, corresponding to plastic strains of ε_p=0.01, ε_p=0.03, ε_p=0.07 and ε_p=0.15. The micro-flat specimens were analyzed through the entire extension of the gauge length to enable the tracking of a selected region. In this approach, conducted for each sample configuration, strain increments were applied to the previously polished specimen using the Deben Microtest stage. After each deformation step, the specimen was transferred to the SEM for EBSD analysis. Once the data for that step was acquired, the sample was removed from the SEM, and the process was repeated for the next strain increment.

2.4.2. *Analysis of microindentation patterns*

A combined approach of Vickers microhardness indentation and EBSD mapping was used in order to investigate the effect of microstructure features, namely grain size and texture, on the local mechanical behavior of the rods. For this purpose, EBSD analyses were conducted at the cross-section of an ∅8-mm rod at the positions described in Fig. 4. The measurement grid comprised five horizontal lines uniformly spaced over a vertical span of 1.6 mm, with individual analysis points positioned at 0.2 mm intervals.

Vickers microhardness indentations were conducted on the same surface areas previously analyzed using EBSD, as represented in Fig. 4, using a Durascan 70 G5 automated system equipped with a micro-Vickers indenter, with a load of 0.1 kg and a holding time of 10 s. The diagonal lengths l_1 and l_2, see Fig. 4, were automatically measured and used as indicators of local strength.

3. Results and discussion

3.1. *Local mechanical properties*

3.1.1. *Effect of texture and grain sizes on indentation patterns*

As investigated by Caroline de Castro et al. [8], the anisotropic characteristic of the CFPed material is observed on the Vickers indentation patterns, with asymmetric diagonal lengths l_1 and l_2 varying depending on the position along the radius. Microstructural features such as grain size and ultrastrong texture can determine the local mechanical properties of the materials, given their effects on grain boundary strengthening and also on ruling the dominant deformation mechanisms. To understand the correlation of the mechanical properties and grain sizes, the grain boundary strengthening was investigated using the Hall-Petch equation [24,40]:

$$\sigma_y = \sigma_0 \;+\; k_y\, d^{-1/2} \quad or \quad H = H_0 \;+\; k_H\, d^{-1/2}, \tag{2}$$

where σ_y represents yield strength, H represents hardness, and σ_0, H_0, k_y and k_H are material-dependent constants.

Given that Vickers microhardness is determined by

$$H = 1.8544 * \frac{F}{l^2}, \tag{3}$$

where F is the applied force, the anisotropic behavior of the material was investigated considering the diagonal lengths separately, and the correlation between the indentation patterns and grain sizes can be assumed as

$$\frac{1}{l_n^2} \propto d^{-1/2}. \tag{4}$$

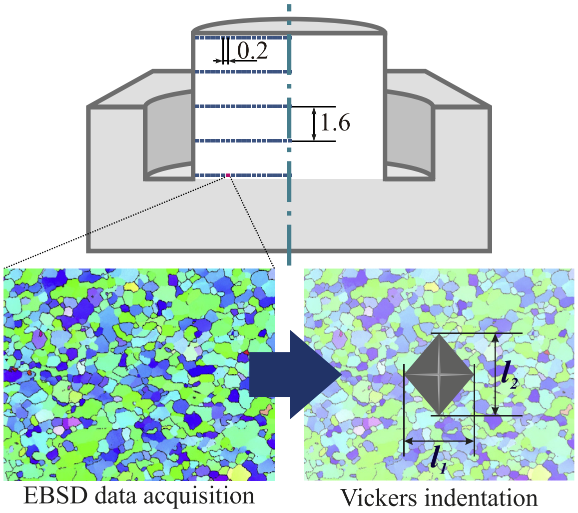

Fig. 4. Schematic representation of the regions selected for EBSD data acquisition, followed by Vickers microhardness testing at the corresponding locations. All dimensions in mm.

Fig. 5 shows the indentation patterns as a function of local grain sizes measured across the rod as indicated in Fig. 4. Although an overall trend of increasing hardness with decreasing grain sizes is observed for l_1 and l_2, the correlation is notably weak due to the significant dispersion of data points for the range of grain sizes present on the specimen. This is further evidenced by the very low R^2 values, indicating a weak statistical fit.

To further understand the influence of microstructural features on the local mechanical behavior, Fig. 5 depicts the correlation between $1/l^2$ with the corresponding local textures, represented by the angle between the c-axis of the hcp structure. In both cases of l_1 and l_2, the data points show two distinct trends, with a sharp transition noted at around $\theta = 75°$. The comparison of R^2 between $\theta < 75°$ with the fitting of grain size data also indicate a substantially greater influence of the local texture over grain size on the material hardness. Furthermore, for $\theta < 75°$, a clear trend of increasing hardness with increasing θ is observed, with R^2 showing statistical significance in comparison to the second part of l_1 and l_2 datasets. This suggests that the local texture significantly influences basal slip, with the progressive increase in θ progressively influencing SF, and may also indicate the activation of further deformation mechanisms such as twinning, as indicated by the sharp transition observed in the plots. For the visualization of the stratified $d^{-1/2}$ data according to the local texture and positions along the radius, please refer to Appendix B, Fig. B.1.

The results depicted in Fig. 5 indicate that, for the range of grain sizes refined during the CFP, local texture plays a more significant role in the determination of the mechanical properties than the grain strengthening effect. Therefore, the following sections focus on understanding the deformation mechanisms activated by the local ultrastrong texture.

3.1.2. Local microtensile behavior

The resulting engineering stress–strain curves at each observed region are depicted in Fig. 6(a). In comparison to the base material, the processed rod exhibits a notable enhancement in overall mechanical properties regarding the ultimate tensile strength (σ_{UTS}), especially in the case of PD-center (53 %) and RD-middle (35 %) specimens, followed by a smaller improvement of 7 % for PD-edge. Additionally, there is a significant increase in yield strength (σ_y), determined as 110 % for RD-middle. In both cases, the increase in strength is primarily attributed to the expressive grain refinement achieved through the CFP. Furthermore, an exceptional improvement of 121 % in terms of elongation at break ($EL\%$) relative to the BM is observed for the PD-edge specimen, which is attributed to the deformation mechanisms triggered by this particular ultrastrong texture as it will be discussed in the following sections.

The significant effect of the local anisotropy on the mechanical behavior observed at each tested region is noticeable in the magnitude of σ_y, σ_{UTS} and $EL\%$. Minor variations on the average grain diameter between the three analyzed specimens ($5.4 \leq \overline{D} \leq 9.1$ μm) might affect the σ_y to some

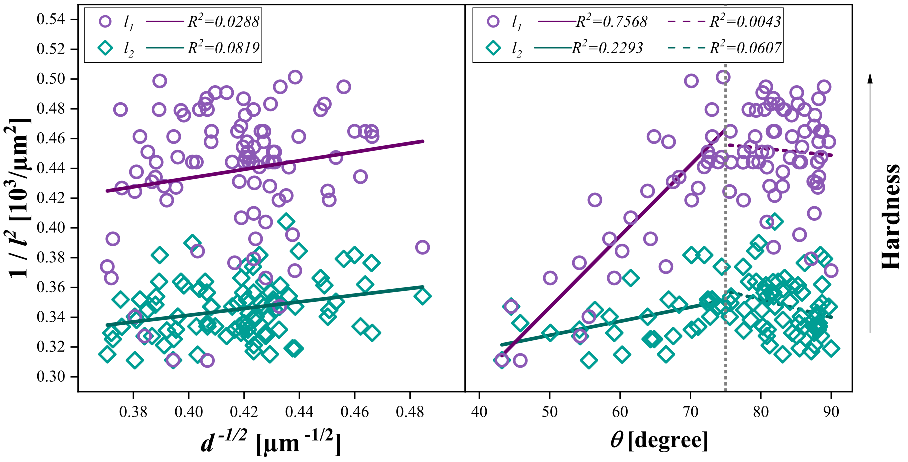

Fig. 5. Indentation patterns ($1/l^2$, l_1 and l_2 according to Fig. 4) as a function of local grain size ($d^{-1/2}$) and local texture (angle of c-axis, θ) for positions collected across the rod. Lines represent the fitted models corresponding to the datasets, with each respective R^2.

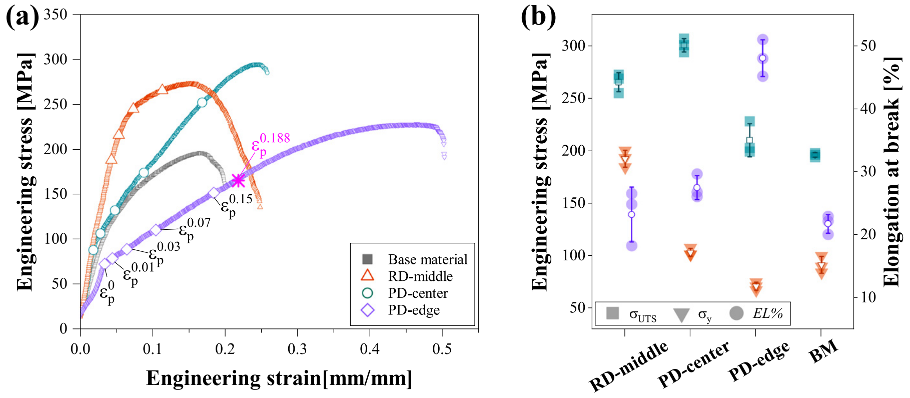

Fig. 6. Local mechanical behavior at the middle along the radial direction (RD-middle), at the center along the plunge direction (PD-center), at the edge along the plunge direction (PD-edge), and base material: (a) exemplary stress–strain curves, and (b) triplicates of yield strength (σ_y), ultimate tensile strength (σ_{UTS}) and elongation at break ($EL\%$) along with the respective average and standard deviation, shown respectively as the open symbols and error bars.

extent due to grain boundary strengthening [22]. However, the particular response of each sample to the deformation behavior is mainly attributed to each of their textures, especially considering the ultrastrong crystallographic orientation of the grains represented by the texture intensity, hinting at specific deformation mechanisms activated by each stress state: (0002) basal planes parallel to the tensile axis (RD-middle), c-axis parallel to the tensile axis (PD-center), and c-axis tilted at 25° in relation to the tensile axis (PD-edge).

The mechanical behavior of AM50 rods produced using CFP reveals notable differences when compared to rods manufactured via traditional methods, like wire drawing [15], rolling [47] or casting [38], see Fig. A.1, highlighting the potential advantages of CFP in tailoring alloy performance. For instance, in a direct comparison, the σ_y determined for the sample at RD-center is only lower than the thin wires manufactured by drawing reported by Dvorsky et al. [15] among the compared techniques. The average σ_{UTS} among the processed material is overall comparable or even higher than the AM50 as-cast and rolled materials studied by Neh et al. [38] and, once again, only lower than the wires reported by Dvorsky et al. [15]. Moreover, the remarkable enhancement in ductility observed in the PD-edge sample significantly exceeds not only the ductility of the AM50 materials used for comparison, but also the elongation at break reported for highly ductile magnesium alloys in the literature, such as AZ91 processed by hard plate rolling ($EL\% = 23$ %) [47] and hot extruded Mg-Gd-Zn-Zr alloy ($EL\% = 36$ %) [33], being comparable only to the Mg-Gr-Mn produced by hot extrusion [50]. For the comparison between the mechanical properties of several Mg alloys and processing techniques, please refer to Appendix A.

3.2. Characterization of local deformation mechanisms under microtensile loading

3.2.1. Grain structure characterization of the specimens

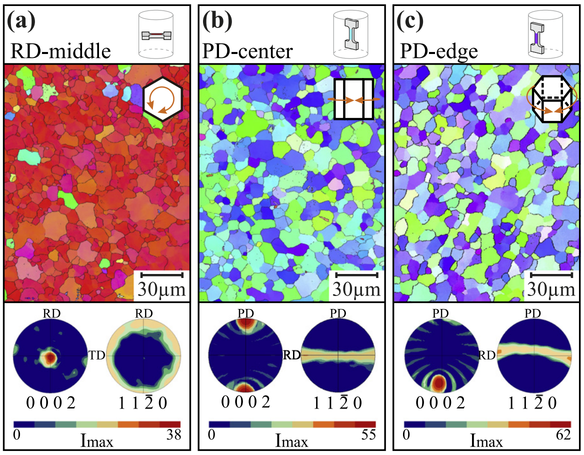

Fig. 7. Initial grain structure of each tracked region on along the gauge length of micro-flat specimens: inverse pole figure maps, pole figures and average grain diameter ($\overline{d}$) analysis for the CFP specimens (a) at the middle along the radial direction (RD-middle), (b) at the center along the plunge direction (PD-center) and (c) at the edge along the plunge direction (PD-edge).

The grain structure of the specimens cut at specific positions of the rods, as shown in Fig. 3(b), is presented in Fig. 7(a–c). The spiral material flow generated during CFP influences the texture formed at each local position along the rod. During the process, the combination of extrusion and stirring components of the material flow leads to particular local shearing conditions. As a consequence, the basal planes of the hcp structure tend to align with the shearing direction, producing a material with ultrastrong local texture, as discussed by de Castro et al. [10]. In all cases, the crystallographic orientation of the grains is ultrastrong in intensity in comparison to other SPD processing of magnesium alloys such as ECAP [23,46] and HPT [51]. On the other hand, the texture intensity values of the samples are in agreement with the crystallographic orientation produced by other friction-based processes of Mg alloys, such as refill FSSW [17], FSW [45] and friction stir processing [29].

Table 2 presents the grain sizes determined along the gauge extension of each specimen ($\overline{D}$) and for the tracked regions of each specimen ($\overline{d}$). In all cases, the variation in terms of $\overline{D}$ was found to be multiple times smaller than the variation in grain size within the single region analyzed, indicating

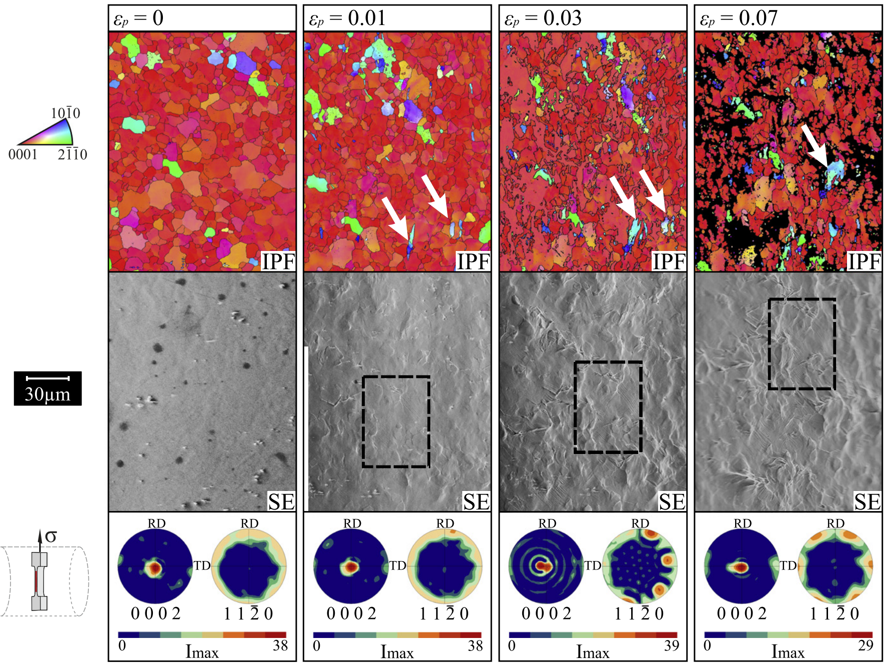

Fig. 8. Grain structure of the specimen with ultrastrong basal texture (RD-middle) at progressive stages of plastic strain (ε_p=0, ε_p=0.01, ε_p=0.03, ε_p=0.07): IPF maps, SE images and pole figures. The white arrows indicate the evolution of twinning along the deformation steps.

Table 2
Average grain diameter along the gauge length ($\overline{D}$) and at the selected region ($\overline{d}$) tracked along the experiment for RD-middle, PD-center and PD-edge.

	$\overline{D}$ [μm]	$\overline{d}$ [μm]
RD-middle	9.1±0.8	10.1±8.2
PD-center	5.4±0.2	5.4±4.1
PD-edge	6.8±0.3	7.2±5.1

that the grain size can be considered statistically consistent throughout the samples. The local grain structure found at the center of the rod along the RD is presented in Fig. 7(b). An ultrastrong basal texture (intensity of 38 mrd) is observed, formed during the process by the alignment of the base planes parallel to the shearing direction, i.e. (0002) // RD. The analysis also indicates that the grain size in the selected region of the RD-middle specimen is $\overline{d}$ = 10.1 ± 8.2 μm. For the specimens taken along the PD, two particular grain structures are identified. At the center (PD-center), Fig. 7(c), fine grains with $\overline{d}$=5.4±4.1 μm show a typical B-fiber texture with ⟨0001⟩ // PD. For the specimen taken at the edge of the rod (PD-edge), as seen in Fig. 7(d), the grain sizes are slightly larger, with $\overline{d}$ = 7.2 ± 5.1 μm. This variation in grain size is expected since the portion of material at the edge of the rod is in close contact with the friction interface between tool and material, promoting slight grain growth due to the exposure to higher temperatures [10]. The texture at this region is defined based on the tilt of ⟨0001⟩ at 25° around the arc between PD-TD, favored by the alignment of the (0002) basal planes with the local shearing conditions. In both cases, the texture intensity is also noted to be ultrastrong, corresponding to 55 and 62 mrd, respectively.

3.2.2. Deformation modes along the radial direction

Fig. 8 shows the inverse pole figure (IPF) maps and secondary electrons (SE) images, which indicate the changes in the grain structure of a particular region along the gauge length observed at progressive strain levels. While a progressive elongation of the grains on the direction of the applied force is observed in all cases, no significant changes in the preferred orientation are observed based on the texture intensity, as the diverging patterns of ε_p=0.03 and ε_p=0.07 can be attributed to the progressively deformed surface and its effect on the quality of the EBSD data acquisition, as seen in Fig. 8. The influence of the increasing straining of the sample is also observed through the evident changes on the surface depicted in the SE images.

The micrographs shown in Fig. 8 follow the evolution of some selected grains, in which the nucleation and growth of extension twins (ET) can be observed. Still, no global occurrence of twinning as a significant deformation mechanism is noticed. This is also supported by the grain boundary misorientation angle depicted in Fig. 9(a), in which the fraction of primary tensile twins is represented by the misorientation angle of 86° in relation to the parent grain. Throughout the investigated history of plastic deformation for this sample, i.e. ε_p= 0 to ε_p=0.07, the variation of the fraction of twin boundaries is not remarkable, ranging from 7.1 % to 9.3 %. This indicates that twinning can be ruled out as a relevant deformation mode in this type of texture.

Fig. 10 (a) shows the Schmid factor maps for the $\{0001\}\langle 11\bar{2}0\rangle$ basal $\langle a\rangle$, $\{1\bar{1}00\}\langle 11\bar{2}0\rangle$ prismatic $\langle a\rangle$, $\{11\bar{2}2\}\langle\overline{11}23\rangle$ second order pyramidal $\langle c+a\rangle$ slip systems and $\{10\bar{1}2\}$ extension twins for the fine-grained microstructures with ultrastrong basal textures. The *SF* maps indicate

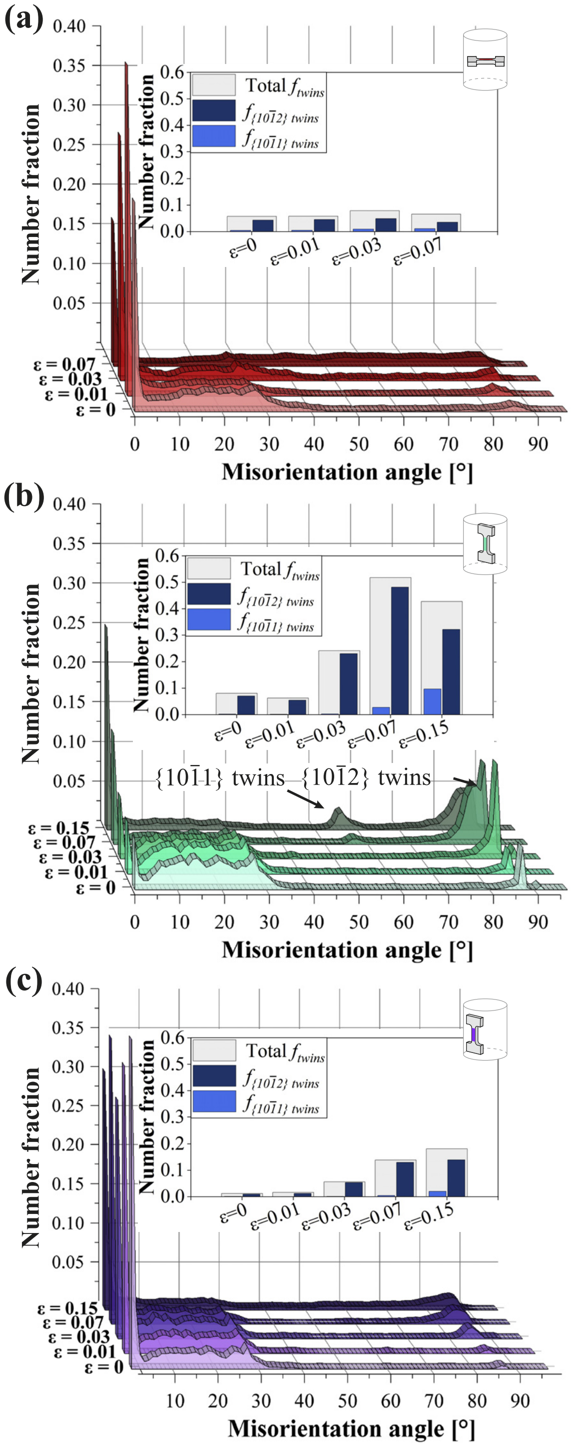

Fig. 9. Grain boundary misorientation angle at progressive stages of plastic strain (ε_p=0, ε_p=0.01, ε_p=0.03, ε_p=0.07) for specimens (a) at the center along the radial direction (RD-middle), (b) at the center along the plunge direction (PD-center) and (c) at the edge along the plunge direction (PD-edge).

that the crystallographic orientation of the grains favors the prismatic ⟨a⟩ dislocations, with a fraction of 92 % of the grains with a high SF associated (≥0.4). Contrarily, the ultrastrong basal texture hinders the activation of basal ⟨a⟩ dislocations, resulting in a fraction of less than 5 % of grains with high SF, a widely-known issue that limits the formability of Mg rolled plates [37] and extruded rods [27] considering that basal slip is the preferred deformation mechanism slip system at room temperatures.

The Schmid's law, see Eq. (1), determines the resolved shear stress (τ_R) of a given grain under a specific loading condition and enables the comprehension of the preferred slip systems ruling the material deformation considering geometric aspects, i.e. the SF. A slip system is considered active when, under specific conditions e.g. loading and/or temperature, the resulting τ_R exceeds τ_{crss} of the given slip system. In this context, the τ_{crss} is associated with the energy required for slip initiation. The reported τ_{crss} values [5] indicate the activation of basal dislocations to be the most energetically favored as τ_{crss} is determined as 20 MPa in contrast to the critical values of 70 and 110 MPa for the prismatic ⟨a⟩ and pyramidal ⟨$c+a$⟩ slip systems. Based on the τ_{crss} values reported in the literature and the σ_{app} associated with ε_p=0, ε_p=0.01 and ε_p=0.07, the critical SF ($SF_{crit}^{\varepsilon_p}$) for the activation of each slip system was calculated, and the results are presented in Table 3. According to the calculation, basal slip is activated for the initial grain structure when $SF^0 \geq 0.09$, in which SF^0 corresponds to the SF at ε_p=0.

Fig. 9 (a) presents the SF values calculated for each individual grain, shown as the corresponding fraction of grains for the basal ⟨a⟩, prismatic ⟨a⟩ and pyramidal ⟨$c+a$⟩ slip systems regarding the ultrastrong basal texture in RD-middle. The $SF_{crit}^{\varepsilon_p}$ values in Table 3 are shown in the plots by the vertical bars. Considering the corresponding $\sigma_{app}^{\varepsilon_p}$ for each strain step observed in the investigation, the fraction of grains with SF^{ε_p} surpassing the calculated $SF_{crit}^{\varepsilon_p}$ is represented by the colored counts in the plots. The results show that, for the tensile loading of microstructures with ultrastrong basal texture, the deformation is ruled by the slip of ⟨a⟩ dislocations, as the fraction of grains with $SF^{\varepsilon_p} \geq SF_{crit}^{\varepsilon_p}$ is 61 % for the basal slip systems, the most energetically favored system as previously discussed, and 96 % for the prismatic ones at ε_p=0. Although the activity of ⟨a⟩ dislocations are favored during the deformation of this grain structure, the fraction of grains exhibiting pyramidal ⟨$c+a$⟩ slip progressively increases with increasing strain.

Fig. 12 (a1-c2) presents the sample's surface over the evaluated strain steps, where the dislocation slip activity is visible. Primary slip bands within the grains are first identified at ε_p=0.01 (a2). The predicted slip traces for each slip system, i.e. basal, prismatic, pyramidal I, and pyramidal II, were calculated based on EBSD data and are represented in (d) by the colored lines, in a similar approach as reported by Yang et al. [49]. According to the calculation of the slip traces potentially active in grain G1, the slip bands indicated as ST$_a$ and ST$_b$ are evidence of the activity of respectively prismatic ⟨a⟩ and pyramidal ⟨a⟩ slip. Besides the ongoing initiation of slip bands with the further straining of the material, at ε_p=0.03 the slip transfer of prismatic ⟨a⟩ dislocations through the G1→G2 grain boundary is progressively activated, identified as ST$_c$ and first observed in (b2) and continuously manifesting as seen in ε_p=0.07. According to the slip traces depicted in (d),

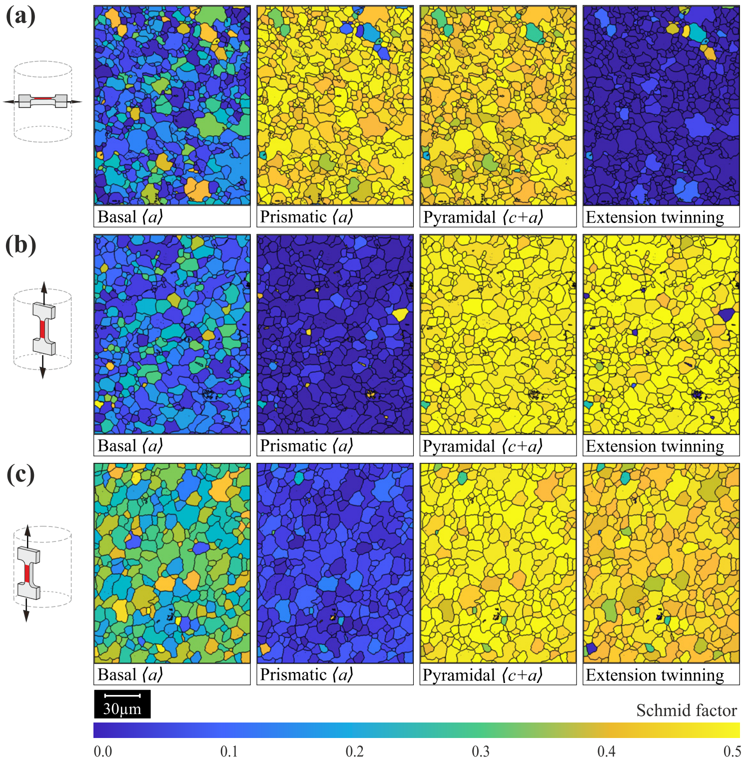

Fig. 10. SF maps of the initial grain structure for $\{0001\}\langle 11\bar{2}0\rangle$ basal $\langle a\rangle$, $\{1\bar{1}00\}\langle 11\bar{2}0\rangle$ prismatic $\langle a\rangle$ and $\{11\bar{2}2\}\langle\bar{1}\bar{1}23\rangle$ second order pyramidal $\langle c+a\rangle$ slip systems, and $\{10\bar{1}2\}$ extension twinning for (a) RD-middle, (b) PD-center and (c) PD-edge.

Table 3
Critical Schmid factor ($SF^{\varepsilon_p}_{crit}\varepsilon$) for the RD-middle specimen calculated from the respective tensile stresses $\sigma^{\varepsilon_p}_{app}$ (in MPa) at ε_p=0, ε_p=0.01, ε_p=0.03 and ε_p=0.07, see Fig. 6(a), considering the τ_{crss} values (in MPa) presented in [5].

	τ_{crss} [5]	σ^{0}_{app}	SF^{0}_{crit}	$\sigma^{0.01}_{app}$	$SF^{0.01}_{crit}$	$\sigma^{0.03}_{app}$	$SF^{0.03}_{crit}$	$\sigma^{0.07}_{app}$	$SF^{0.07}_{crit}$
basal $\langle a\rangle$	20	215	0.09	244	0.08	265	0.08	250	0.08
prismatic $\langle a\rangle$	70	215	0.33	244	0.29	265	0.26	250	0.28
pyramidal $\langle c+a\rangle$	110	215	0.51	244	0.45	265	0.42	250	0.44

ST$_c$ denotes the activity of pyramidal $\langle a\rangle$ slip system. The occurrence of slip bands followed by slip transfer is reported in other studies on hcp materials, such as magnesium [52] and titanium [28] alloys. As the strain progresses in the material, dislocations pile up at the grain boundaries, increasing the local shear stress. Slip transfer will occur at a given grain boundary if two criteria are simultaneously fulfilled, being (i) high SF values of the incoming and outgoing slip planes, and (ii) high geometric compatibility [28]. The geometric compatibility factor (m') [32], is defined as

$$m' = \cos\kappa \ \cos\psi \tag{5}$$

where κ is the angle between the incoming and outgoing slip direction and ψ is the angle between the pair of normal slip planes, as represented in Fig. 1. The analysis of m' for each specimen investigated points to a high probability for dislocation slip transfer to the adjacent grains. The ultrastrong orientation of the grains results in a low angle ψ between the incoming and outcoming dislocation slip planes (0002), i.e. $cos\psi \approx 1$, and a relatively low angle between the slip directions of the two pairs of planes (κ), which is assumed to be of a maximum of 30°, i.e. $cos\kappa > 0.86$ taking into account the symmetry of the hcp basal plane and the misorientation angle distribution of Fig. 9(a). Therefore, the ultrastrong texture of RD-middle favors the slip transfer behavior as the slip systems of neighboring grains are well-aligned, which is described as a mechanism to enhance the ductility [52].

3.2.3. Deformation modes along the center of the rod

The IPF maps, pole figures and twin boundary maps of a selected area on specimen PD-center is depicted in Fig. 13, observed at ε_p=0, ε_p=0.01, ε_p=0.03, ε_p=0.07 and ε_p=0.15. The activation of twinning as a deformation mechanism is not noticed at the initial steps of deformation ($\varepsilon_p \leq$0.03). The SF maps for ε_p=0, see Fig. 10, hint at the activity of $\langle c+a\rangle$ slip systems. The ultrastrong B-fiber texture at PD-center indicates that basal slip may be restricted for the tensile stress applied parallel to the c-axis, as the basal planes are perpendicular to the tensile axis, leading to only 0.4 % of the grains exhibiting high SF ($\geq$ 0.4). The $\langle a\rangle$ slip is also restricted for the prismatic slip, with only 1.3 % of the grains associated with high SF. The analysis of SF shows that for the tensile

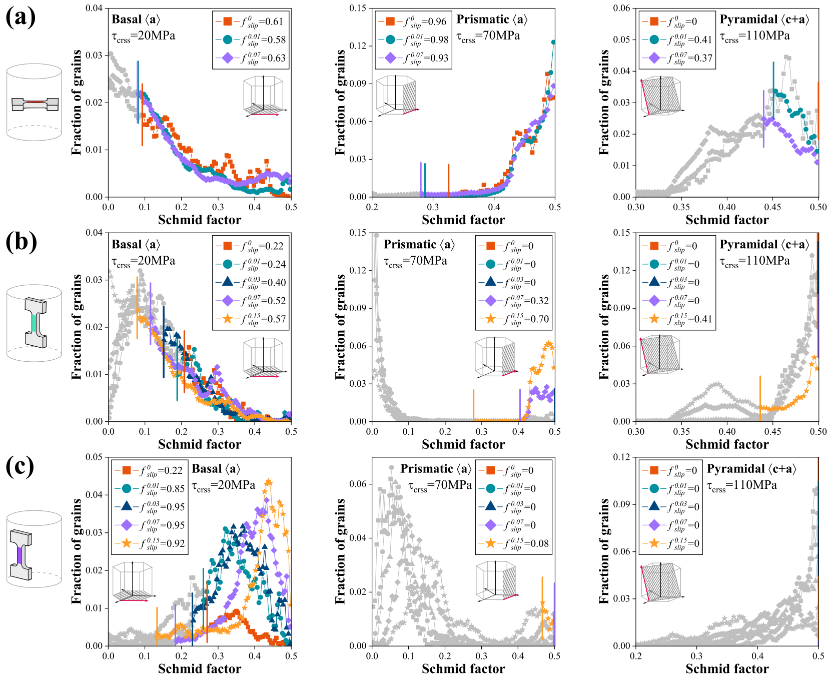

Fig. 11. Ultrastrong (a) basal texture (RD-middle), (b) B-fiber texture parallel to PD (PD-center) and (c) B-fiber texture tilted at 25° in relation to PD (PD-edge): *SF* grain fraction distribution for $\{0001\}\langle 11\bar{2}0\rangle$ basal $\langle a\rangle$, $\{1\bar{1}00\}\langle 11\bar{2}0\rangle$ prismatic $\langle a\rangle$ and $\{11\bar{2}2\}\langle\bar{1}\bar{1}23\rangle$ second order pyramidal $\langle c+a\rangle$, depicting the fraction of grains with sufficient stress to activate each slip systems ($f^{\varepsilon p}_{slip}$) as the colored portions of the plots. The fraction of grains with activated dislocation slip ($f^{\varepsilon p}_{slip}$) is indicated in the legend.

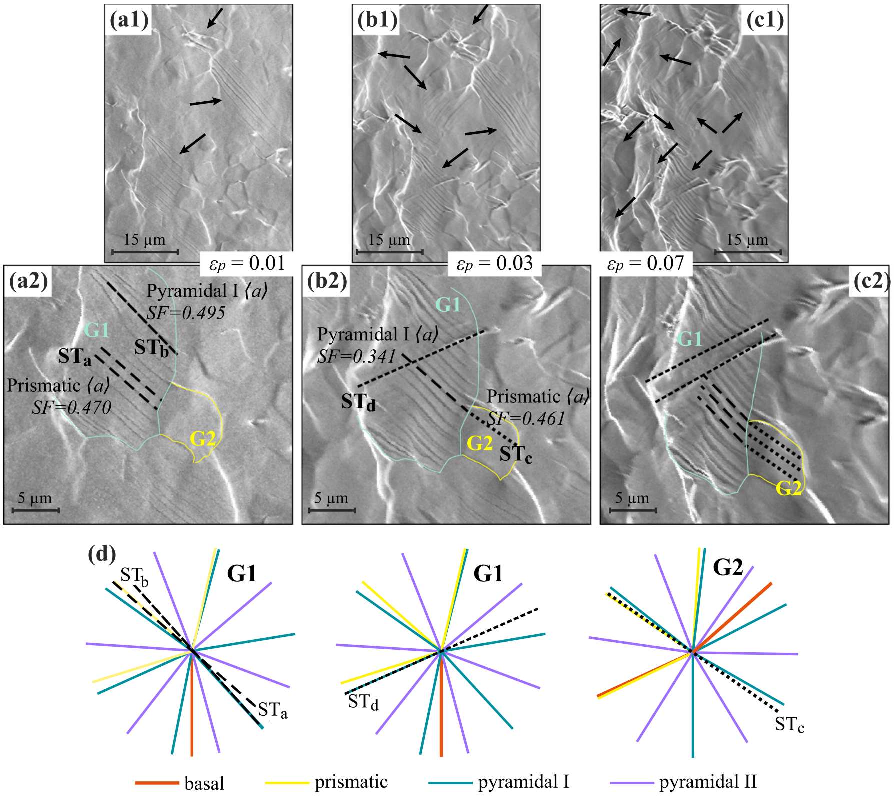

Fig. 12. SEM secondary electron images of the surface of the RD-middle specimen (a1-c1) and selected areas in higher magnification showing the slip traces activity (a2-c2) at ε_p=0.01, ε_p=0.03, ε_p=0.07. The calculated slip traces (ST_a, ST_b, ST_c, ST_d) of different slip systems for grains G1 and G2 are presented in (d), determined based on EBSD data. The slip systems are represented by the red (basal), yellow (prismatic), green (pyramidal I) and purple (pyramidal II) lines.

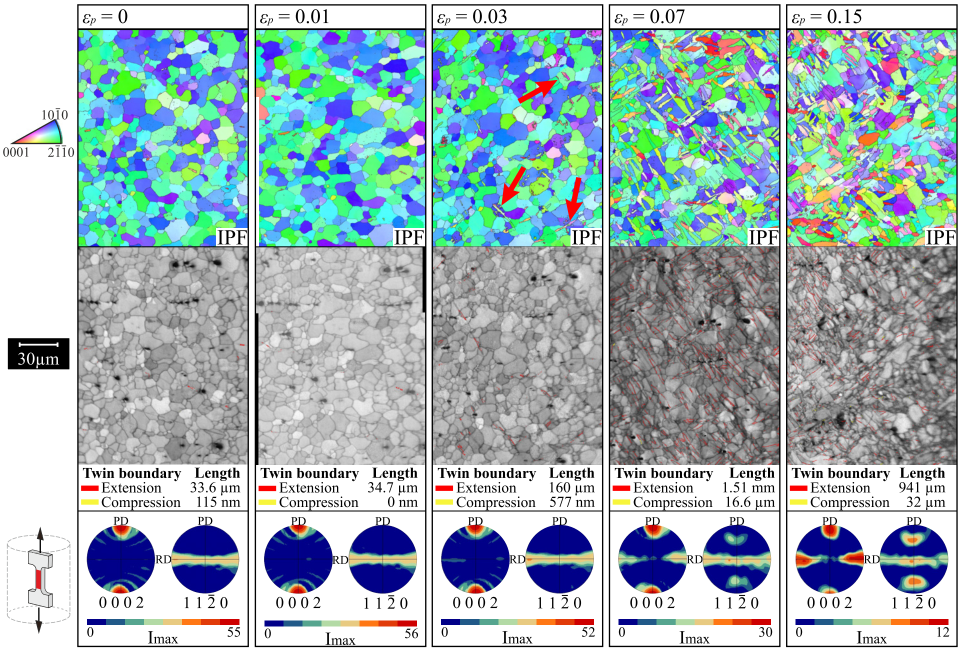

Fig. 13. Grain structure of the specimen with ultrastrong B-fiber texture (PD-center) at progressive stages of plastic strain (ε_p=0, ε_p=0.01, ε_p=0.03, ε_p=0.07 and ε_p=0.15): IPF maps, twin boundary maps and pole figures. The nucleation of ET is exemplary pointed by the red arrows at ε_p=0.03.

Table 4
Critical Schmid factor ($SF_{crit}^{\varepsilon_p}$) for the PD-center specimen calculated from the respective tensile stresses $\sigma_{app}^{\varepsilon_p}$ (in MPa) at ε_p=0, ε_p=0.01, ε_p=0.03, ε_p=0.07 and ε_p=0.15, see Fig. 6(a), considering the τ_{crss} values (in MPa) presented in [5].

	τ_{crss} [5]	σ_{app}^{0}	SF_{crit}^{0}	$\sigma_{app}^{0.01}$	$SF_{crit}^{0.01}$	$\sigma_{app}^{0.03}$	$SF_{crit}^{0.03}$	$\sigma_{app}^{0.07}$	$SF_{crit}^{0.07}$	$\sigma_{app}^{0.15}$	$SF_{crit}^{0.15}$
basal $\langle a\rangle$	20	96	0.21	106	0.19	132	0.15	173	0.12	252	0.08
prismatic $\langle a\rangle$	70	96	*	106	*	132	*	173	0.40	252	0.28
pyramidal $\langle c+a\rangle$	110	96	*	106	*	132	*	173	*	252	0.44

* The slip system cannot be activated.

loading of this particular texture, the activity of $\langle c+a\rangle$ dislocations are favored as 98 % of the grains present high SF. Nonetheless, the analysis of the slip systems considering the τ_{crss} presented in the literature, as seen in Fig. 11(b), indicates that basal slip is favored, with the fraction of grains meeting the conditions to activate the basal dislocation increasing from 22 % for ε_p=0 to 57 % for ε_p=0.15. The calculation of $SF_{crit}^{\varepsilon_p}$, see Table 4, denotes that the prismatic and pyramidal slip systems can only be activated at the highest levels of stress/strain observed. Compared to the previous analysis of the RD-middle sample, the ultrastrong B-fiber texture causes significantly lower dislocation activity, with a reduced fraction of grains capable of deforming via dislocation slip. In contrast, SF maps depicted in Fig. 11(b) shows that more than 98 % of the grains are associated to high SF regarding extension twinning, hinting that this may be a dominant mechanism governing the deformation in this type of texture.

In addition to the limited activity of basal $\langle a\rangle$ dislocations, the plasticity of the PD-center is also heavily influenced by twinning. The twinning activity can be assessed by the analysis of the misorientation angle of the grain boundaries, depicted in Fig. 9(b), in a similar approach as investigated by Suhuddin et al. [45]. At the two initial stages, ε_p=0 and ε_p=0.01, a comparable fraction of $\{10\bar{1}2\}$ ET associated to the misorientation angle of 86° in relation to the parent grain is observed. This fraction of twin boundaries is attributed to remnants of the CFP process and/or artifacts from the sample manufacturing procedure. From ε_p=0.03, $\{10\bar{1}2\}$ ET is activated as a deformation mode, which is denoted by the increase in the peak intensity and peak broadening, resulting in the fraction of ET indicated in the corresponding graph inset in Fig. 9(b). While the increase in peak intensity implies the nucleation of new twins and/or the propagation of existing ones, the peak broadening is associated with the growth of newly formed grains within the twin boundaries, causing a shift in the misorientation of the ET boundaries [44]. The substantial activity of ET reaches its maximum at ε_p=0.07, where 48 % of the grain boundaries corresponding to ET twin boundaries. Together with the ET, the occurrence of $\{10\bar{1}1\}$ contraction twins (CT), identified by a misorientation of 56° in relation to the parent grain, is noted to a limited fraction of boundaries starting at ε_p=0.03. In addition to the tensile stresses applied during the test, internal compressive stresses acting perpendicular to the loading direction may result from the Poisson effect [31]. It is worth noting that the deformation modes identified in this study for the B-fiber texture un-

Table 5
Resolved shear stress (τ_R^{ET}) for extension twinning, calculated based on the average SF related to the ultrastrong B-fiber texture (PD-center) along ε_p=0, ε_p=0.01, ε_p=0.03, ε_p=0.07 and ε_p=0.15 and correspondent stresses ($\sigma_{app}^{\varepsilon_p}$).

	ε_p^0	$\varepsilon_p^{0.01}$	$\varepsilon_p^{0.03}$	$\varepsilon_p^{0.07}$	$\varepsilon_p^{0.15}$
SF	0.48	0.48	*0.48*	0.47	0.47
σ_{app} [MPa]	96	106	*132*	173	252
τ_R^{ET} [MPa]	46	51	*63*	81	118

der tensile loading parallel to the c-axis align with findings from molecular dynamics simulations of a Mg single crystal [34], which concluded that the dominant mechanisms are a combination of basal slip and twinning. The activity of ET as the main deformation mechanism throughout the progressive stages of deformation is further supported by the twin boundary maps shown in Fig. 13, where the corresponding boundary lengths exhibit a trend consistent with the fractions observed in the misorientation angle plots in Fig. 9.

The evolution of twinning activity after ε_p=0.03 is also noticed in the pole figures of Fig. 13, which indicate significant changes in terms of the preferred orientation of the grains. These modifications are quantitatively assessed through changes in the texture intensity, which ranges from 55 mrd for the first three observations and decreases significantly to 12 mrd at ε_p=0.15. Furthermore, the progressive rise of new peaks in the pole figure indicates the growth of new grains at the ET boundaries with preferred orientation of the c-axis parallel to the RD varying around 45° in relation to the TD.

The resolved shear stress for the ET is presented in Table 5. The $\tau_R^{\varepsilon_p}$ values were calculated according to Eq. (1) for each step of observation based on the $\sigma_{app}^{\varepsilon_p}$ determined in Fig. 6, using the average SF obtained from Fig. 11(b). As concluded above, the ET are activated at around $\varepsilon_p \approx$0.03. Therefore, the critical resolved shear stress for the activation of ET in the AM50 rods addressed in the current study, τ_{crss}^{ET}, can be estimated to be around 63 MPa. This value can be considered a reliable estimation as it is consistent with the results obtained by Gharghouri et al. [20], where τ_{crss}^{ET} was experimentally determined to be between 65 and 75 MPa for a Mg-7.7Al (at.%) alloy using an in-situ neutron diffraction approach.

3.2.4. Deformation modes along the edge of the rod

Fig. 14 depicts the grain structure evolution during the stages of deformation under tensile stress applied to a specimen with a ultrastrong texture and a c-axis orientation of 25°. As for the sample with the B-fiber texture parallel to the PD, twins are first observed at $\varepsilon_p = 0.03$. Based on the grain misorientation distribution shown in Fig. 9(c), the twins activated at $\varepsilon_p = 0.03$ correspond to grain boundaries with a misorientation of 86°, indicating the occurrence of $\{10\bar{1}2\}$ ET. Nonetheless, although this texture present a high SF for ET as calculated in Fig. 10(c), the notable ductility of this material is not primarily attributed to twinning, as it accommodates significantly less strain compared to the PD-center texture, with less than 15 % of the grain boundaries reorienting into ET boundaries over the deformation.

The assessment of slip activity for the basal and prismatic $\langle a\rangle$ and pyramidal $\langle c+a\rangle$ dislocations throughout the deformation stages is illustrated in Fig. 11(c), considering the SF_{crit} calculated based on the τ_{crss} presented in the literature [5] and the σ_{app} obtained from the experiment and listed in Table 6. The plots indicate that the conditions for activating the $\langle c+a\rangle$ slip were not met, similar to the case with the prismatic dislocations. In opposition, the slip of basal $\langle a\rangle$ dislocations can be activated under the applied σ_{app} as the 25°-tilt enhances the SF associated with this grain crystallographic orientation. Moreover, the effect of the 25° angle in enhancing basal slip, which consequently impacts the material's ductility, is evident when comparing the maps of undeformed specimens shown in Fig. 10. For the PD-edge sample, over 43 % of the grains exhibit calculated SF values greater than 0.3, compared to less than 15 % for the RD-middle and only 5.5 % for the PD-center. A similar effect of c-axis tilt on ductility enhancement is observed in strongly textured AZ31 produced via ECAP route B$_\mathrm{C}$, compared to the B-fiber texture developed through route A as reported by Gzyl et al. [23]. According to the study, and consistent with the present PD-edge observations, the improved ductility can be attributed to the favorable SF for the activation of basal slip inherent to this crystallographic orientation. Nonetheless, the comparison of the $EL\%$ ratio between the B-fiber and tilted c-axis texture components in strongly (ECAP, 0.612) and ultrastrongly (current study, 0.562) textured materials indicates that the higher texture intensities achieved through CFP promote the activation of a larger fraction of energetically favorable grains for basal slip. This effect, together with the more favorable slip transfer associated with higher values of m' in ultrastrong textures, leads to a further enhancement in ductility.

The increase in $f_{slip}^{\varepsilon_p}$ values shown in Fig. 11(c) demonstrates that the applied strain drastically impacts the activity of the basal $\langle a\rangle$ slip system. The analysis of the pole figures shows progressive changes in the crystallographic orientation of the grains, as depicted in Fig. 15(a), where the angle θ is determined between the base planes normal and plunge direction (or analogously to the tensile axis). Representative examples of grains exhibiting this effect are presented in Appendix C (see Fig. C.1) for further analysis. Lattice rotation-mediated plasticity is reported in the literature as a progressive rotation of grains from their original orientation due to slip activity occurring on a specific slip system [36]. It is also noted as a significant deformation mode in fcc [35] and hcp [19] materials. A similar effect of lattice rotation on the material structure is also presented by Gao et al. [19], where the presence of γ/γ' two-phase structure allows the visualization of the rotated domains in a single-crystal superalloy.

As ε_p increases, a trend for the change in θ is observed, as it progressively converges to an angle of 45°. This indicates that the basal planes reorient to the angle of 45°, reaching maximum SF, as depicted in Fig. 15(b). This reorientation of the basal planes can be directly associated with the activity

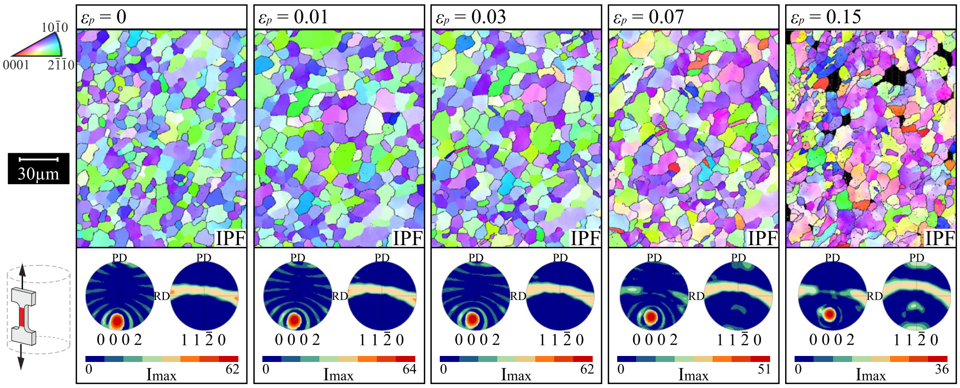

Fig. 14. Grain structure of the specimen with ultrastrong B-fiber texture tilted at 25° in relation to the arc between PD-TD (PD-edge) at progressive stages of plastic strain (ε_p=0, ε_p=0.01, ε_p=0.03, ε_p=0.07 and ε_p=0.15): IPF maps and pole figures.

Table 6
Critical Schmid factor ($SF^{\varepsilon_p}_{crit}$) for the PD-edge specimen calculated from the respective tensile stresses $\sigma^{\varepsilon_p}_{app}$ (in MPa) at ε_p=0, ε_p=0.01, ε_p=0.03, ε_p=0.07 and ε_p=0.15, see Fig. 6(a), considering the τ_{crss} values (in MPa) presented in [5].

	τ_{crss} [5]	σ^{0}_{app}	SF^{0}_{crit}	$\sigma^{0.01}_{app}$	$SF^{0.01}_{crit}$	$\sigma^{0.03}_{app}$	$SF^{0.03}_{crit}$	$\sigma^{0.07}_{app}$	$SF^{0.07}_{crit}$	$\sigma^{0.15}_{app}$	$SF^{0.15}_{crit}$
basal $\langle a\rangle$	20	74	0.27	77	0.26	87	0.23	109	0.18	150	0.13
prismatic $\langle a\rangle$	70	74	*	77	*	87	*	109	*	150	0.47
pyramidal $\langle c+a\rangle$	110	74	*	77	*	87	*	109	*	150	*

* The slip system cannot be activated.

of the basal slip, as observed in Fig. 11(c). To assess the effect of lattice rotation on the mechanical behavior of the material, the ε_p corresponding to reorientation of the lattice towards optimum SF was determined based on a polynomial fitting presented in Fig. 15(b). According to the results, the basal planes are expected to be aligned at θ=45° at around $\varepsilon_p = 0.188$.

Fig. 15 (c) illustrates the relative contribution of basal slip activity and lattice rotation to the deformation evolution in the ultrastrong texture with a tilted c-axis, where τ_R/τ_{crss} provides a reasonable estimate of basal slip activation. This evaluation was based on the calculated basal slip activation rates under two conditions: one assuming a constant crystallographic orientation (θ=24.7°), and the other considering the lattice rotation phenomenon as shown in Fig. 15(a). While a progressively higher basal slip activity is inherently associated with the initial texture (area highlighted in orange), resulting from a relatively high Schmid factor (SF=0.38), the contribution of lattice rotation to the observed plasticity rapidly increases, ultimately being responsible to contribute to an additional 50 % of slip activation as SF values approaches 0.5, as observed on the area highlighted in purple. This particular deformation behavior corresponds to the quasi-linear segment of the plots depicted in Fig. 6(a) up to $\varepsilon_p = 0.188$, where the stress-strain response transition to a non-linear behavior. Therefore, beyond this point, basal slip becomes the primary deformation mechanism alone for the remaining strain as the grains reach the optimal orientation for maximum SF.

The identification of lattice rotation as one major deformation mode in PD-edge enables its correlation with the material's exceptional elongation at break. In contrast, both the σ_y and σ_{UTS} are the lowest among the investigated materials given the ease with which the deformation mechanisms can occur. To the best of our knowledge, no investigations regarding the lattice rotation mechanism in ultrastrong textured materials have been reported, which share more similarities with single crystals under tensile stress in terms of deformation mechanisms rather than with polycrystalline materials that have random or weak texture. The comparison of the mechanical behavior of PD-center/PD-edge specimens with single-crystals of a superalloy under tensile loading [19] shows a similar trend in the variation of σ_y, σ_{UTS}, and $EL\%$ with θ, indicating a corresponding decrease in strength and increase in ductility as θ increases.

The as-cast AM50 alloy is not typically classified among Mg alloys with high ductility. However, a notable enhancement in room-temperature ductility was observed for the ultrastrong texture of the PD-edge specimen ($EL\%\approx$49 %). This value is comparable to the $EL\%$ reported for extruded Mg alloys designed for high ductility, such as Mg-0.18 % at. Nd [30] and Mg-Gr-Mn [50], both of which slightly exceed 50 %. This highlights the potential of CFP for enhancing ductility through the tailoring of ultrastrong textures.

The analysis of m' for the dominant slip modes at RD-middle, PD-center and PD-edge, as depicted in Fig. 16, provides insight into the higher ductility exhibited by the latter. With a higher geometric compatibility factor found for the PD-edge texture, the transmission of dislocations across the grain boundaries is favored, resulting in a much lower strain hardening rate and, consequently, a higher capacity to accommodate strain.

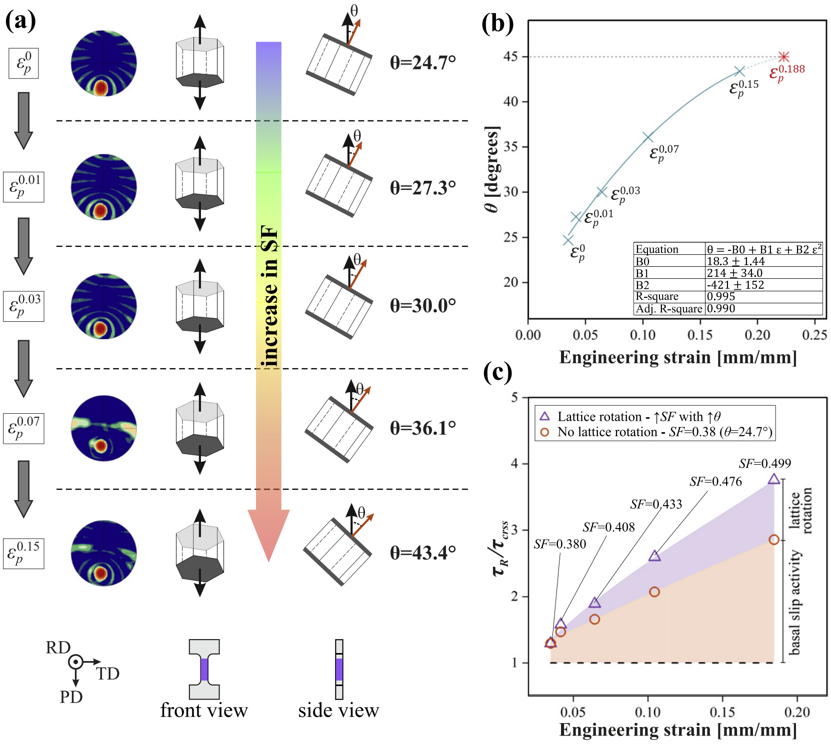

Fig. 15. Lattice rotation mediated plasticity in PD-edge material: (a) reorientation of crystallographic texture along the strain, (b) evolution of the angle between the normal basal planes and the tensile axis (θ) and engineering strain and (c) plots of τ_{rss}/τ_{crss} highlighting the role of specific deformation mechanisms in plastic strain evolution.

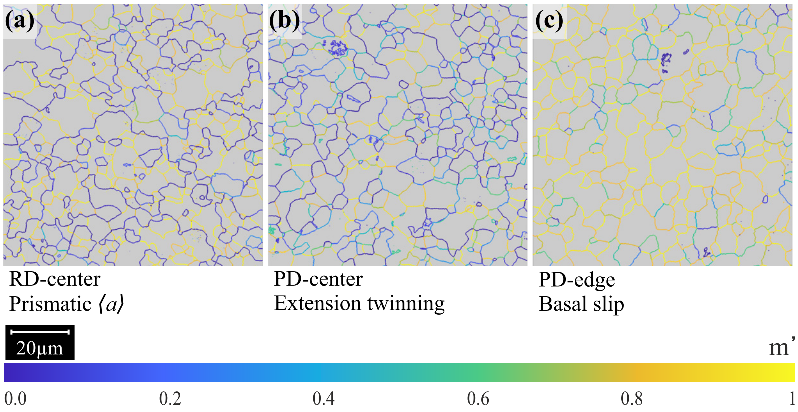

Fig. 16. Geometric compatibility factor (m') for the dominant slip system corresponding to (a) RD-middle, (b) PD-cente and (c) PD-edge.

4. Conclusions

In this study, the local mechanical behavior of rods produced via CFP was determined based on grain structure characterization combined with the analysis of indentation patterns across the rod and an approach involving quasi-in-situ microtensile experiments using specimens taken at three distinct positions along the rod. The major findings are summarized below.

- Microstructural analysis of the CFPed AM50 rod indicates that grain size has a limited influence on local mechanical properties. In contrast, variations in crystallographic texture across different regions of the rod play a dominant role, as they govern the active deformation mechanisms associated with each distinct ultra-strong texture.
- The main mechanism ruling the deformation of the RD-middle sample under tensile loading was determined as the prismatic $\langle a \rangle$ dislocation slip. Additionally, the ultra-strong basal texture favors slip transfer given the high m' between the grains in the vicinity, improving the limited ductility of this texture. In terms of properties, RD-middle exhibits a high yield strength (σ_y), mainly associated with the activation of less energetically favorable slip systems.

- The ultrastrong B-fiber texture at the PD-center favors extension twinning as the dominant deformation mode under tensile loading along the c-axis. Compared to RD-middle, the higher twinning activity facilitates greater strain accommodation, resulting in the highest observed ultimate tensile strength (σ_{UTS}) in the study, along with a comparatively elevated elongation percentage ($EL\%$).
- The exceptional $EL\%$ at the rod's edge is associated with the ultrastrong B-fiber texture featuring a 25° c-axis tilt. This crystallographic orientation leads to enhanced basal slip activity facilitated by progressive lattice rotation. With increasing ε_p, the θ angle associated with the basal planes progressively rotates toward the maximum SF, where basal $\langle a \rangle$ dislocation activity is at its highest.

Understanding the relationship between local mechanical behavior and grain structure in CFPed rods enables material optimization for specific applications and loading conditions, despite current process limitations (maximum rod length of 20 mm). This includes the use of biocompatible Mg alloys for small implants, such as high-strength bone screws and ductile cardiovascular stents.

Data availability

The obtained data of this research is online available at Zenodo (https://doi.org/10.5281/zenodo.17611842).

Declaration of competing interest

The authors declare that they have no known competing financial interests or personal relationships that could have appeared to influence the work reported in this paper.

CRediT authorship contribution statement

Camila Caroline de Castro: Conceptualization, Methodology, Formal analysis, Investigation, Validation, Writing – original draft, Writing – review & editing, Visualization. **Ting Chen:** Formal analysis, Investigation, Validation, Writing – review & editing. **Diogo de Campos Fernandes:** Investigation, Writing – review & editing. **Benjamin Klusemann:** Resources, Supervision, Writing – review & editing.

Acknowledgements

The authors acknowledge the funding by the Deutsche Forschungsgemeinschaft (DFG, German Research Foundation) - project number 544306307. We would like to acknowledge Prof. Dr. Norbert Hort and Mr. Günter Meister from Helmholtz-Zentrum Hereon, Institute of Metallic Biomaterials, for providing, casting, and heat-treating the AM50 ingots.

Appendix A. Comparison between mechanical properties of AM50 rods with Mg alloys processed via traditional processing methods

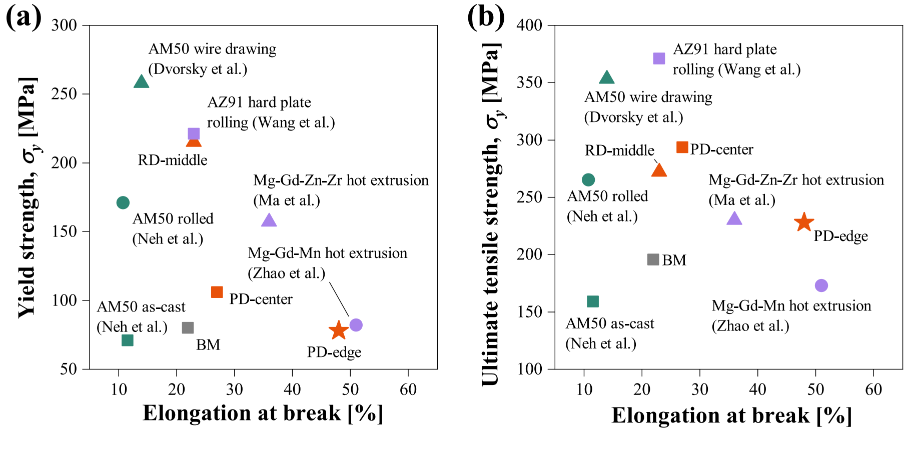

Fig. A.1. Yield strength (σ_y), ultimate strength (σ_{UTS}) and elongation at break ($EL\%$) of Mg materials under tensile strength: base material (BM) and specimens at the center along the radial direction (RD-center), at the center along the plunge direction (PD-center) and at the edge along the plunge direction (PD-edge) (a), comparison to AM50 produced by different processing routes (as-cast [38], rolling [38] and wire drawing [15]) (b) and comparison to high ductility Mg alloys (AZ91 hard plate rolling [47], Mg-Gd-Zn-Zr hot extrusion [33] and Mg-Gd-Mn hot extrusion [50].

Appendix B. Correlation between grain size and indentation patterns according to positions along the rod radius and crystallographic texture

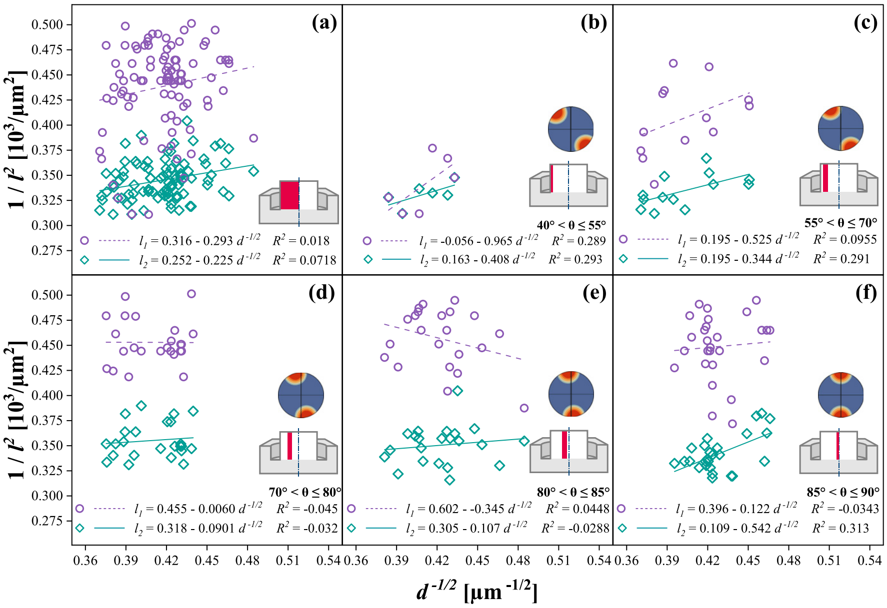

Fig. B.1. $1/l^2$ (l_1 and l_2, according to Fig. 4) as a function of grain size ($d^{-1/2}$) (a) at positions along the rod and (b-f) grouped according to the local crystallographic texture.

Appendix C. Progressive lattice rotation observed in selected grains during deformation.

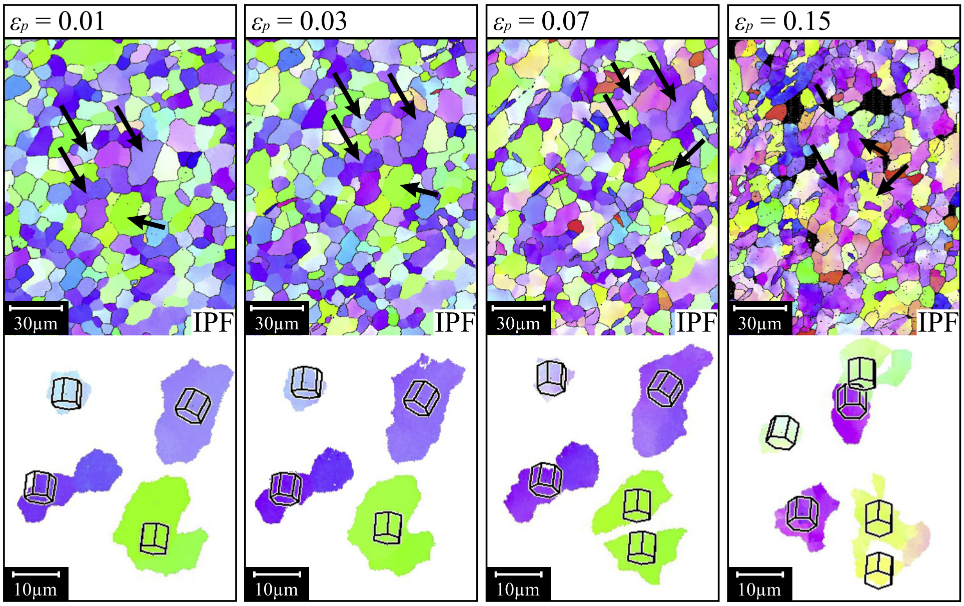

Fig. C.1. Progressive lattice rotation during deformation at progressive staves of plastic strain (ε_p=0.01, ε_p=0.03, ε_p=0.07, ε_p=0.15) observed in the selected grains indicated by the arrows.

References

[1] F. Bachmann, R. Hielscher, H. Schaeben, Ultramicroscopy 111 (12) (2011) 1720–1733, doi:10.1016/j.ultramic.2011.08.002.

[2] D. Baffari, G. Buffa, D. Campanella, L. Fratini, A.P. Reynolds, J. Manufact. Process. 29 (2017) 41–49, doi:10.1016/j.jmapro.2017.07.010.

[3] M.R. Barnett, Mater. Sci. Eng. A 464 (1-2) (2007) 1–7, doi:10.1016/j.msea.2006.12.037.

[4] M.R. Barnett, Mater. Sci. Eng. A 464 (1-2) (2007) 8–16, doi:10.1016/j.msea.2007.02.109.

[5] N. Bertin, C.N. Tomé, I.J. Beyerlein, M.R. Barnett, L. Capolungo, Int. J. Plast. 62 (2014) 72–92, doi:10.1016/j.ijplas.2014.06.010.

[6] J. Bohlen, S. Meyer, B. Wiese, B.J.C. Luthringer-Feyerabend, R. Willumeit-Römer, D. Letzig, Materials 13 (2) (2020), doi:10.3390/ma13020391.

[7] W.D. Callister, D.G. Rethwisch, Materials Science and Engineering: An introduction, 9th ed., Wiley, United States, 2014.

[8] C. Caroline de Castro, T. Chen, D. de Campos Fernandes, B. Klusemann, Mater. Res. Proc. 54 (2025) 1777–1785, doi:10.21741/9781644903599-191.

[9] C.C. de Castro, A.M. Neves, B. Klusemann, J. Magnes. Alloy 12 (6) (2024) 2298–2311, doi:10.1016/j.jma.2024.04.002.

[10] C.C. de Castro, J. Shen, J. Fernandez, B. Klusemann, J. Mater. Process. Tech. 318 (2023) 118018, doi:10.1016/j.jmatprotec.2023.118018.

[11] J. Chen, R. Sun, G. Li, M. Fang, G. Xu, M. Zhang, J. Li, Met. Mater. Int. 28 (2022) 2677–2690, doi:10.1007/s12540-021-01158-5.

[12] T. Chen, B. Fu, J. Shen, U.F.H.R. Suhuddin, B. Wiese, Y. Huang, M. Wang, J.F. dos Santos, J.P. Bergmann, B. Klusemann, J. Magnes. Alloy 12 (2) (2024) 516–529, doi:10.1016/j.jma.2023.10.007.

[13] T. Chen, B. Fu, F.H.R.S. Uceu, T. Shen, G. Li, E. Maawad, J. Shen, J.F. dos Santos, J.P. Bergmann, B. Klusemann, J. Mater. Sci. Technol. (In press) (2025), doi:10.1016/j.jmst.2025.01.026.

[14] N.M. Della Ventura, S. Kalácska, D. Casari, T.E.J. Edwards, A. Sharma, J. Michler, R. Logé, X. Maeder, Mater. Design 197 (2021) 109206, doi:10.1016/j.matdes.2020.109206.

[15] D. Dvorsky, J. Kubasek, E. Jablonska, J. Lipov, D. Vojtech, Mater. Technol. 34 (14) (2019) 838–842, doi:10.1080/10667857.2019.1638638.

[16] F.R. Elsayed, N. Hort, M.A. Salgado-Ordorica, K. Kainer, Mater. Sci. Forum 690 (2011) 65–68, doi:10.4028/www.scientific.net/MSF.690.65.

[17] B. Fu, J. Shen, U.F.H.R. Suhuddin, T. Chen, J.F. dos Santos, B. Klusemann, M. Rethmeier, Scr. Mater. 203 (2021) 114113, doi:10.1016/j.scriptamat.2021.114113.

[18] W.M. Gan, M.Y. Zheng, H. Chang, X.J. Wang, X.G. Qiao, K. Wu, B. Schwebke, H.G. Brokmeier, J. Alloys Compd. 470 (1-2) (2009) 256–262, doi:10.1016/j.jallcom.2008.02.030.

[19] X. Gao, Z. Zhang, L. Liu, C. Tao, Mater. 17 (6) (2024), doi:10.3390/ma17061368.

[20] M.A. Gharghouri, G.C. Weatherly, J.D. Embury, J. Root, Philos. Mag. A: Physics of Condensed Matter, Structure, Defects and Mechanical Properties 79 (7) (1999) 1671–1695, doi:10.1080/01418619908210386.

[21] A. Gokhale, R. Sarvesha, T.S. Guruprasad, S.S. Singh, J. Jain, Mater. Sci. Eng. A 816 (2021) 141258, doi:10.1016/j.msea.2021.141258.

[22] B. Guan, Y. Xin, X. Huang, P. Wu, Q. Liu, Acta Mater. 173 (2019) 142–152, doi:10.1016/j.actamat.2019.05.016.

[23] M. Gzyl, A. Rosochowski, S. Boczkal, L. Olejnik, Mater. Sci. Eng. A 638 (2015) 20–29, doi:10.1016/j.msea.2015.04.055.

[24] E.O. Hall, Proc. Phys. Soc. 64 (Section B) (1951) 767, doi:10.1088/0370-1301/64/9/303.

[25] L. Hou, T. Wang, R. Wu, J. Zhang, M. Zhang, A. Dong, B. Sun, S. Betsofen, B. Krit, J. Mater. Sci. Technol. 34 (2) (2018) 317–323, doi:10.1016/j.jmst.2017.02.005.

[26] International, A. (2024). ASTM E8M: Standard Test Methods for Tension Testing of Metallic Materials. 10.1520/E0008

[27] S. Kleiner, P.J. Uggowitzer, Mater. Sci. Eng. A 379 (1-2) (2004) 258–263, doi:10.1016/j.msea.2004.02.020.

[28] H. Li, K. Wang, R. Xin, Mater. Charact. 211 (2024), doi:10.1016/j.matchar.2024.113863.

[29] F.C. Liu, Z.Y. Ma, M.J. Tan, Metall. Mater. Trans. A: Phys. Metall. Mater. Sci. 44 (8) (2013) 3947–3960, doi:10.1007/s11661-013-1746-3.

[30] G. Liu, J. Zhang, G. Xi, R. Zuo, S. Liu, Acta Mater. 141 (2017) 1–9, doi:10.1016/j.actamat.2017.09.006.

[31] S. Liu, D. Kent, N. Doan, M. Dargusch, G. Wang, Bioact. Mater. 4 (1) (2019) 8–16, doi:10.1016/j.bioactmat.2018.11.001.

[32] J. Luster, M.A. Morris, Metall. Mater. Trans. A 26 (7) (1995) 1745–1756, doi:10.1007/BF02670762.

[33] Y. Ma, C. Liu, S. Jiang, Y. Wan, Y. Gao, Z. Chen, Z. Liu, J. Mater. Res. Technol. 27 (2023) 1509–1525, doi:10.1016/j.jmrt.2023.10.023.

[34] Z.C. Ma, X.Z. Tang, Y. Mao, Y.F. Guo, Mater. 14 (4) (2021) 1–16, doi:10.3390/ma14040733.

[35] T. Mayama, K. Aizawa, Y. Tadano, M. Kuroda, Comput. Mater. Sci. 47 (2) (2009) 448–455, doi:10.1016/j.commatsci.2009.09.009.

[36] S. Nagarajan, R. Jain, N.P. Gurao, Mater. Charact. 180 (2021) 111405, doi:10.1016/j.matchar.2021.111405.

[37] T. Nakata, S. Kamado, J. Magnes. Alloy 11 (11) (2023) 3992–4010, doi:10.1016/j.jma.2023.08.006.

[38] K. Neh, M. Ullmann, R. Kawalla, Mater. Today: Proc. 2 (2015) S219–S224, doi:10.1016/j.matpr.2015.05.017.

[39] J.F. Nie, K.S. Shin, Z.R. Zeng, Microstructure, Deformation, and Property of Wrought Magnesium Alloys, vol. 51, Springer US, 2020, doi:10.1007/s11661-020-05974-z.

[40] N.J. Petch, J. Iron and Steel Inst. 174 (1953) 25–28.

[41] L. Rath, C. Chan, U. Suhuddin, H. Buresch, T. Ebel, B. Klusemann, Processability of Mg-Gd powder via friction extrusion, in: Proceedings of the 14th International Conference on the Technology of Plasticity - Current Trends in the Technology of Plasticity, in: Lecture Notes in Mechanical Engineering, Vol. 1, 2024, pp. 431–441, doi:10.1007/978-3-031-41023-9_44.

[42] F. Sayari, R. Roumina, R. Mahmudi, M.M. Hoseini-athar, P. Hedström, J. Alloys Compd. 908 (2022) 164407, doi:10.1016/j.jallcom.2022.164407.

[43] C. Schilling, J.F. Dos Santos, Method and Device for Linking at Least Two Adjoining Work Pieces by Friction Welding, EP1230062, 2000.

[44] S.S.A. Shah, M. Liu, A. Khan, F. Ahmad, M.R. Abdullah, X. Zhang, S. Xu, Z. Peng, J. Magnes. Alloy 12 (6) (2024) 2201–2230, doi:10.1016/j.jma.2024.04.035.

[45] U.F.H.R. Suhuddin, S. Mironov, Y.S. Sato, H. Kokawa, C.W. Lee, Acta Mater. 57 (18) (2009) 5406–5418, doi:10.1016/j.actamat.2009.07.041.

[46] C. Wang, A. Ma, J. Sun, H. Liu, H. Huang, Z. Yang, J. Jiang, J. Alloys Compd. 793 (2019) 259–270, doi:10.1016/j.jallcom.2019.04.202.

[47] H.Y. Wang, Z.P. Yu, L. Zhang, C.G. Liu, M. Zha, C. Wang, Q.C. Jiang, Sci. Rep. 5 (5988) (2015) 1–9, doi:10.1038/srep17100.

[48] S. Xu, J. Wang, Acta Mater. 229 (2022) 117805, doi:10.1016/j.actamat.2022.117805.

[49] B. Yang, C. Shi, R. Lai, D. Shi, D. Guan, G. Zhu, Y. Cui, G. Xie, Y. Li, A. Chiba, J. LLorca, Scr. Mater. 214 (2022) 114648, doi:10.1016/j.scriptamat.2022.114648.

[50] T. Zhao, Y. Hu, Y. Wang, Y. Dai, T. Zheng, Z. Li, K. Li, B. He, C. Zhang, F. Pan, J. Magnes. Alloys (2023), doi:10.1016/j.jma.2023.10.004.

[51] R. Zheng, J.P. Du, S. Gao, H. Somekawa, S. Ogata, N. Tsuji, Acta Mater. 198 (2020) 35–46, doi:10.1016/j.actamat.2020.07.055.

[52] B. Zhou, Y. Li, L. Wang, H. Jia, X. Zeng, Acta Mater. 227 (2022), doi:10.1016/j.actamat.2022.117662.

[53] X. Zhou, H. Xia, J. Zhang, G. Zeng, X. Lu, X. Chen, X. Pang, J. Li, J. Guo, J. Mater. Sci. Technol. 212 (2025) 237–250, doi:10.1016/j.jmst.2024.03.086.

[54] X. Zhou, Y. Yao, J. Zhang, X. Chen, W. Huang, J. Pan, H. Wang, M. Weng, J. Mater. Sci. Technol. 70 (2021) 156–167, doi:10.1016/j.jmst.2020.08.054.